Computational Study of the Advancing-Side Lift-Phase Problem

R. Steijl,* G. N. Barakos,† and K. J. Badcock‡
University of Liverpool, Liverpool, England L63 3GH, United Kingdom

The prediction of airloads and the corresponding structural response in high-speed forward flight of rotors poses a significant challenge to predictive rotorcraft aeromechanics methods. One of the issues identified in the flight test data of the Puma and Black Hawk aircraft is the phase difference between the minimum lift coefficient and the minimum of the blade pitch on the advancing side of the rotor during high-speed forward flight. This is commonly referred to as the advancing-side lift-phase delay. In the present work, the unsteady three-dimensional flowfield on the advancing side of a helicopter rotor is analyzed using computational fluid dynamics in an attempt to quantify contributions to the preceding effect. Time-dependent two-dimensional computational fluid dynamics simulations of blade sections with combined pitch/freestream Mach number oscillation were carried out to isolate the contribution to the phase difference of pitch angle and Mach number variations in the absence of the complex rotor-induced flowfield, sideslip, and rotor blade dynamics. The results for the freestream Mach number oscillations show that the lift coefficient lags the Mach changes at outboard stations, but this effect is reduced for combined pitch/Mach number oscillations. Finite span and sideslip contributions to the phasing were quantified by investigating the chordwise extent of supersonic flow on the advancing side for two nonlifting rotors in high-speed flight. Finally, the UH-60A rotor in high-speed forward flight was considered. By comparing results for rigid blades with results for a prescribed blade torsional deflection, the contribution of the blade torsion to the advancing-blade lift phasing was also quantified. Furthermore, rigid-blade simulations with different flapping schedules demonstrated the sensitivity of the lift phasing to trim-state variations. It was found that Mach number effects are dominant and the lift phasing depends primarily on the encountered Mach number and pitch schedule. Further, the elastic torsional deflection of the blades effectively changes the pitch schedule of the blade sections and also plays a role in the phasing of the lift and pitching moment coefficients.

Nomenclature

$\mathcal{R}$	=	rotor aspect ratio, R/c
a_∞	=	freestream speed of sound, m/s
C_N	=	section normal force coefficient (blade section axes)
C_p	=	pressure coefficient, $(p - p_\infty)/q_\infty$
C_T	=	rotor thrust coefficient, $T/[\rho_\infty(\Omega R)^2 \pi R^2]$
c	=	(mean) rotor chord, m
k	=	$\omega c/(2 U_\infty)$
M_r	=	relative Mach number, $M_H[r/R \cos(\lambda) + \mu \sin(\psi - \lambda)]$
M_{tip}	=	rotational Mach number, $\Omega R/a_\infty$
$M^2 C_p$	=	$(p - p_\infty)/(\frac{1}{2}\gamma p_\infty)$
M_∞	=	freestream Mach number
p_∞	=	freestream pressure, Pa
q_r	=	relative dynamic pressure, Pa, $\frac{1}{2}\rho_\infty[\Omega r + U_\infty \sin(\psi - \lambda)]^2$
q_∞	=	freestream dynamic pressure, Pa, $\frac{1}{2}\rho_\infty U_\infty^2$
R	=	rotor radius, m
r	=	radial coordinate along the rotor blade, m
U_∞	=	freestream velocity, m/s
β_0	=	rotor coning, deg
β_{1c}, β_{1s}	=	first harmonic flap coefficients, deg
θ_0	=	rotor collective, deg
θ_{1c}, θ_{1s}	=	first harmonic pitch coefficients, deg
λ	=	(local) blade sweep angle, deg
μ	=	rotor advance ratio, M_∞/M_{tip}
ρ_∞	=	freestream density, kg/m³
σ	=	rotor solidity, $N_{\text{blades}}/\pi \mathcal{R}$
ψ	=	blade azimuth (0 deg at the rear of the rotor disk), deg.
Ω	=	rotor rotation rate, rad/s
ω	=	oscillation frequency, rad/s

*Research Associate, Computational Fluid Dynamics Laboratory, Department of Engineering; R.Steijl@Liverpool.ac.uk.
†Senior Lecturer, Computational Fluid Dynamics, Department of Engineering; G.Barakos@Liverpool.ac.uk.
‡Professor, Computational Fluid Dynamics Laboratory, Department of Engineering; K.J.Badcock@Liverpool.ac.uk.
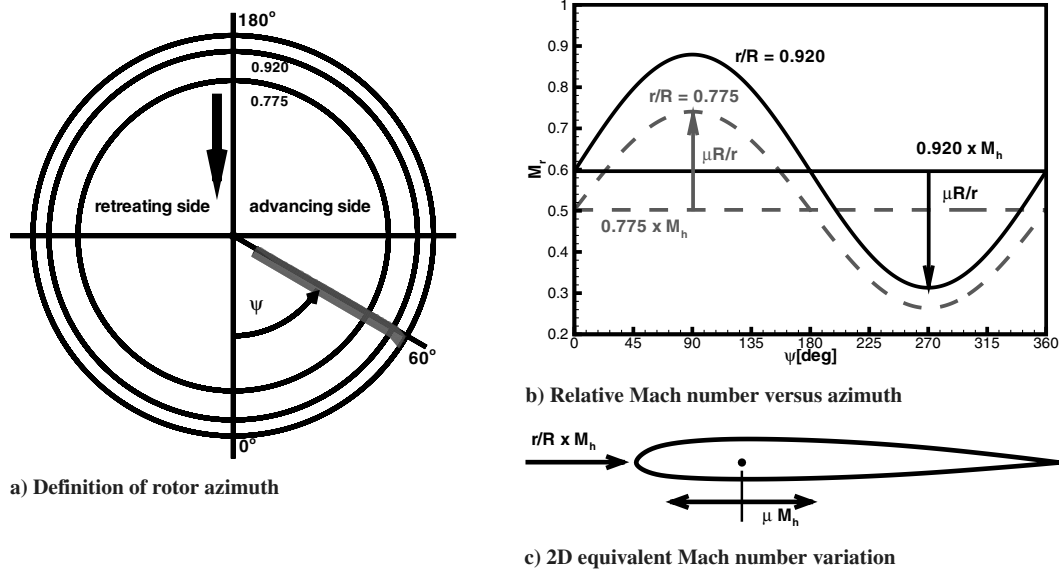
I. Introduction

THE numerical prediction of the time-dependent aerodynamic airloads and the corresponding structural response of a helicopter rotor in high-speed forward flight poses significant challenges to predictive methods. Such methods usually combine an aerodynamic model (Euler, Navier–Stokes, potential, or reduced-order) with structural modeling of the rotor or full helicopter (modal- or finite-element-based) and a helicopter trimming method. Only recently have Euler- or Navier–Stokes-based predictions become feasible for routine use, and for design applications, reduced-order aerodynamic models are still the common approach in the industry. To validate predictive methods and to provide data for design purposes, there have been many efforts to measure rotor blade pressures, blade motions, and deformations in flight conditions [1] as well as in wind tunnels [2,3].

Figure 1 presents a schematic of a helicopter rotor blade in forward-flight conditions. The velocity component in the chordwise direction experienced by a section at a radial position r/R, denoted as relative velocity in the present work, includes contributions due to blade rotation and the freestream velocity component. The resulting periodic variation of the relative Mach number around the azimuth is presented in Fig. 1b. A trimmed level flight involves a reduction of the rotor blade pitch on the advancing side of the rotor disk and a similar increase on the retreating side to account for the relative velocity variation. This cyclic pitch is required to balance the rotor forces and moments, and it increases with increasing forward-flight speed. As a result, a substantial part of the rotor airloads is carried by

a) Definition of rotor azimuth

b) Relative Mach number versus azimuth

c) 2D equivalent Mach number variation

Fig. 1   Notation for advancing-side aerodynamics.

the front and rear parts of the rotor disk. In most high-speed flight conditions, the outboard blade stations may even experience negative lift on the advancing side, the increased relative velocity of which may result in transonic flow conditions with shock formation. On the retreating side, the reduced relative velocity and the associated pitch increases may then lead to low-speed flows with (dynamic) stall. Furthermore, the strong vortices in the rotor wake play an important role in the overall aerodynamic performance of the rotor. The blades undergo a periodic flapping motion, balancing the unsteady airloads and the inertial loads applied to them. The rigid-body motion of the blades, as well as the elastic deformation, are tightly coupled to the rotor aerodynamics. A detailed account of the challenging problems related to the analysis of helicopter rotors is described in the review paper of Conlisk [4], among others.

Figure 2 presents the sectional lift at 86.5% rotor radius for the UH-60A helicopter in high-speed forward flight at two thrust levels [5]. The peak of the negative lift at the outboard part of the blade on the advancing side occurs at about azimuth $\psi = 120$ deg. The minimum of the blade sectional pitch is, however, at an azimuth angle of about 85 deg. The data from the U.S. Army/NASA UH-60A

Airloads Program [1] (discussed in more detail in Sec. I.A), using recent corrections [6], show a similar trend. This phase difference requires further investigation.

Despite the significant development effort, predictive methods based on lower-order aerodynamic models have been found to give poor predictions in high-speed flight, showing two key discrepancies compared with experimental data [7]:

1) The phase prediction of advancing-blade lift in high-speed forward flight fails to show the advancing-blade phase delay.

2) The prediction of the sectional pitching moment is poor, both in phasing and magnitude.

These observations were made for different helicopters and for a range of blade designs. This discrepancy between predicted advancing-side airloads and experimental data is commonly referred to as the *advancing-side lift-phase problem*.

Reduced-order aerodynamic models are typically based on assumptions that become invalid in cases of high rotor loading and/or high-speed (i.e., when viscous or compressibility effects become the dominant effect). In addition, the irrotational-flow assumption requires the use of a wake model for potential-flow methods that concentrate the vorticity of the vortical wake of lifting rotors in panels, segments or blobs. Two types of wake models are widely used in rotorcraft aerodynamics: the prescribed wake, in which the wake geometry is fully predefined and the strengths of the vortex singularities are the unknowns, and the free-wake model, in which the wake geometry is relaxed, along with the solution of the vortex strengths. A significant limitation of both models is that the global structure of the wake is defined by the model (i.e., the number and position of the trailing vortices or vortex sheets emanating from the trailing edge). For high-speed and or high-lift cases, the wake geometry may be significantly different from that in economic cruise conditions.

Recent computational fluid dynamics (CFD) investigations using aerodynamic modeling based on the Euler or Navier–Stokes equations resulted in better predictions that were in better agreement with experiments [8,9]. The main reason behind this improvement is the ability of CFD to predict the three-dimensional unsteady aerodynamics of the outboard part of the blade on the advancing side. The strong nose-down pitching moments associated with these conditions cannot be resolved by potential-flow or lifting-line models. Furthermore, the elastic twist response of the blade to these nose-down moments is a major factor in the phasing of the advancing-side lift [9].

Based on the preceding, the aim of the present study is to use CFD to study the unsteady aerodynamic phenomena that determine the phasing of the advancing-side lift and the phasing and magnitude of the sectional pitching moments.
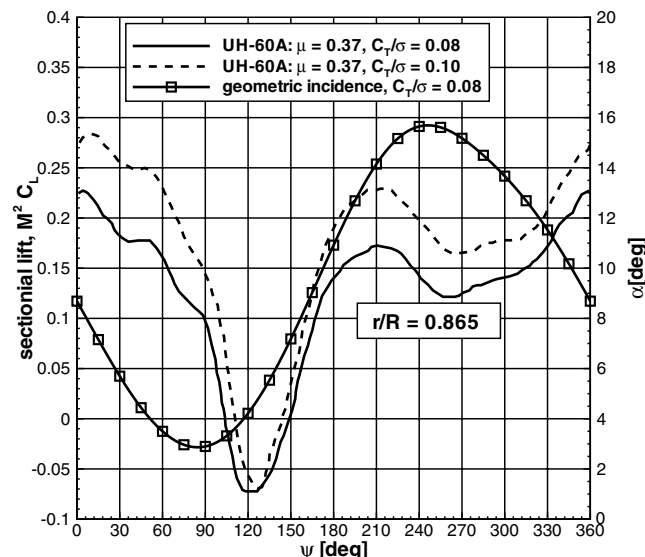

Fig. 2   Sectional lift at two radial stations of the UH-60A main rotor in high-speed forward flight indicating the well-documented lift-phase delay on the advancing side in high-speed flight. Experimental data were obtained from Coleman and Bousman [5].

Table 1 Conditions at several radial stations of the UH-60A rotor blade ($M_{\text{tip}} = 0.64$ and $\mu = 0.368$)

Station, %	Section	$M_{\text{tip}} \cdot (r/R)$	$\mu/(r/R)$	$M_{\psi=90\,\text{deg}}$	$M_{\psi=270\,\text{deg}}$	k
77.5	SC1095R8	0.494	0.475	0.732	0.260	0.0416
86.5	SC1095	0.554	0.425	0.790	0.318	0.0373
92.0	SC1095	0.587	0.400	0.825	0.353	0.0351

A. Experimental Data for High-Speed Forward Flight of Rotors

The aerodynamics and airloads of the UH-60A main rotor in hover conditions were investigated using a 1:5.73-scale wind-tunnel model in the Duits–Nederlandse Windtunnel (DNW) by Lorber and his coworkers [2]. The wind-tunnel model was both Mach and aeroelastically scaled; that is, the model rotation rate was scaled up relative to the full-scale rotor to match the tip Mach number, whereas the model structure was tailored to approximate the aeroelastic characteristics of the full-scale rotor. The rotor blades were equipped with pressure sensors at ten radial stations. During further experiments [3], the rotor was also tested at forward-flight conditions covering a range of advance ratios ($0.07 < \mu < 0.36$). The rotor was trimmed to have zero first-harmonic flapping. For level flight at $\mu = 0.30$, Lorber [3] reported the following observations for the advancing-side aerodynamics:

1) At the outboard blade stations, sonic velocities were attained for $90\,\text{deg} < \psi < 170\,\text{deg}$, with a maximum chordwise extent of supersonic flow at $\psi = 115\,\text{deg}$.

2) Blade-vortex interactions occurred for the outer 60% of the blade for $0\,\text{deg} < \psi < 60\,\text{deg}$.

3) Strong nose-down pitching moments induced an elastic-blade twist near the tip of up to 4 deg at $\psi = 170\,\text{deg}$.

Relevant to the present work are also data concerning investigations of airfoil sections with oscillatory pitching and oscillatory translation motions. However, data in the literature are typically obtained at low speeds and low Reynolds numbers. The objective of these tests is typically the investigation of (dynamic) stall of airfoils. Such experiments with oscillating airfoils were reported by Favier et al. [10], and experiments with oscillatory freestream schedules include those of Krause and Schweitzer [11] and Morikawa and Grönig [12].

B. Review of Previous CFD and Aeroelastic Investigations

The aeromechanics of the advancing side of a rotor in high-speed forward flight were previously investigated by various researchers using an approach that decoupled the aerodynamics and the structural responses of the rotor blades (e.g., [13,14]). Such investigations focused on the UH-60A rotor, using experimental data from the U.S. Army/NASA UH-60A Airloads Program. The measured airloads and rotor control angles were used to predict the structural response of the rotor. Based on the computed blade deformations and measured rotor control angles, the aerodynamic model was used to predict the airloads on the rotor. For a CFD-based aerodynamic model, the computed vibratory rotor airloads were in good agreement with the measured airloads [14], showing the validity of the structural model as well as the CFD method. However, as mentioned previously, the predicted steady and 1/rev blade-normal forces show significant differences compared with the experimental data. Based on the computed blade deformations and measured rotor control angles, various investigations were conducted to assess the validity of reduced-order aerodynamic models commonly used in comprehensive analysis methods, such as table-lookup methods and indicial methods for the computation of unsteady 2D sectional aerodynamics for a prescribed blade incidence schedule. Significant shortcomings were found in predicting advancing-side blade lift, pitching moment, and vibratory lift for these reduced-order models, confirming previous findings [7]. For the airfoils of the UH-60A rotor (i.e., SC1095 and SC1095R8), data from CFD simulations were used to derive section-specific constants for the Leishman–Beddoes model for a range of Mach numbers. It was found that the improved indicial functions did not significantly improve the advancing-blade aerodynamic airloads [13]. The influence of 3D unsteady effects such as crossflow were also investigated using improved indicial functions [13] and CFD [14]. The indicial functions were extended to include additional terms representing the effect of the sideslip angle. The model parameters were determined using data from 3D CFD simulations of constant-section wings (SC1095R8 section) at sideslip conditions. Sideslip angles of up to 15 deg were considered. For the vibratory lift predictions, inclusion of the additional terms was found to have little effect in comparison with the 2D indicial functions. The 1/rev lift and the pitching moment magnitudes, however, improved consistently, whereas the phase errors in the pitching moment remained. A CFD analysis of the effect of blade-tip sweep [14] suggests increased effects of hysteresis in aerodynamic loads for unsteady pitch oscillations.

C. Outline of the Present Investigation

The objective of the present paper is to analyze the unsteady effects that determine the aerodynamic loads, both in magnitude and phasing, on the advancing side of the rotor in high-speed forward flight.

The first step of the present investigation isolates the effect of the Mach number and pitch oscillations experienced by rotor blade sections in forward flight. Two stations along the UH-60A rotor blade are of particular interest in view of the experimental data from the U.S. Army/NASA UH-60A Airloads Program [1]: the first one at 77.5% radius (SC1095R8 section) and the second at 92.0% radius (SC1095 section). For the high-speed forward flight considered here (i.e., with $M_{\text{tip}} = 0.638$ and $\mu = 0.368$), the radial stations are modeled in 2D, as summarized in Table 1.

In the second part of the investigation, the flowfield and pressure distributions of a nonlifting rotor at high-speed forward flight were investigated. In this case, the blade experiences the combined effect of Mach number variations and crossflow and tip-relief (finite span) effects. These effects can be analyzed in the absence of a vortical wake and induced flowfield.

The final part of the study consists of an analysis of the blade loading of the UH-60A main rotor in high-speed forward flight at moderate lift conditions with a representative trim state. Rigid blades were first considered, though subsequently, elastic torsion was also imposed.

II. CFD Solution Method: Validation

The CFD results in the present work were obtained from simulations conducted using the in-house Helicopter Multi-Block (HMB) CFD solver, which solves the Reynolds-averaged Navier–Stokes equations on block-structured grids using a cell-centered finite volume method for spatial discretization. An implicit time-integration method is employed, and the resulting linear systems of equations are solved using a preconditioned generalized conjugate gradient method. For unsteady simulations, the dual-time-stepping method is used, which is based on Jameson's implicit pseudo-time-integration approach. The formulation for rotor hover and forward-flight simulations were described previously [15]. The HMB solver has so far been validated for many rotorcraft flows, including blade–vortex interaction [16], 3D dynamic stall [17], and hovering and forward-flying rotors [15]. Further validation for hovering and forward-flying rotors is also presented in this paper.
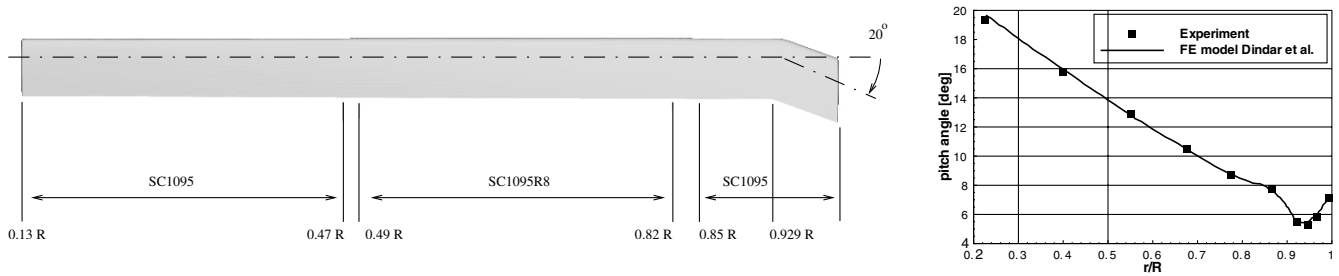
Fig. 3   Geometry of UH-60A rotor blade; nonlinear twist according to Dindar et al. [18].
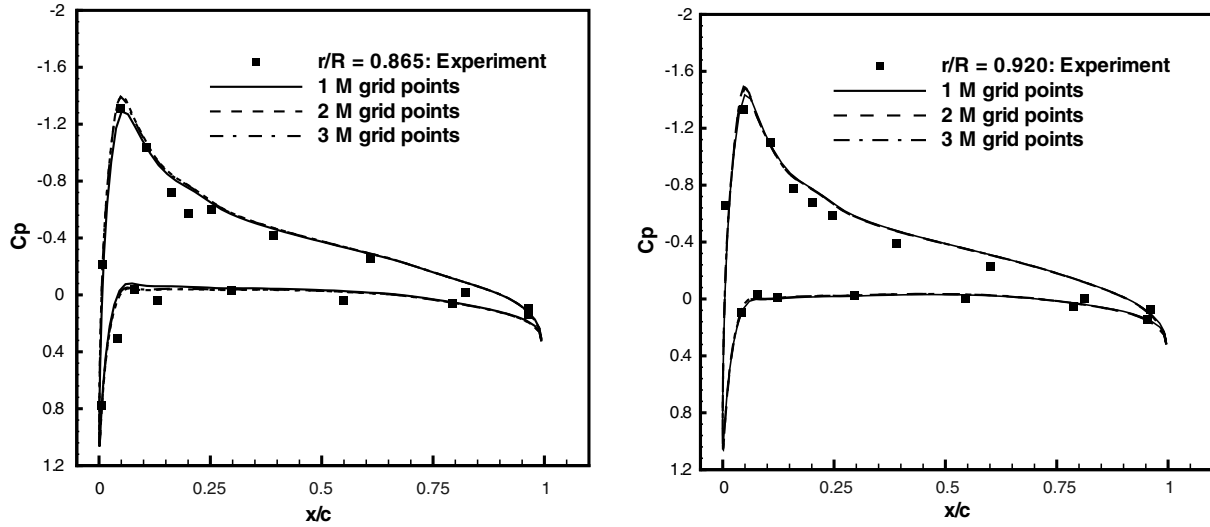

Fig. 4   Validation results for the UH-60A rotor in hover; sectional C_p distributions at two radial stations; $M_{tip} = 0.628$; 10.47-deg collective and 2.31-deg coning.

A.   UH-60A Model Rotor in Hover

The case under consideration is a hovering four-bladed UH-60A rotor at a thrust of $c_T/\sigma = 0.085$, collective of 10.47 deg, and coning angle of 2.31 deg (details are shown in Fig. 3), following the description of Dindar et al. [18] for the nonlinear twist distribution. Figure 4 presents a comparison of the computed chordwise c_p distribution with published experimental data from Lorber [3]. The inviscid CFD simulations (using single-blade periodic grids) were carried out using three mesh densities. The results obtained on all grids are in good agreement with the experimental data. The predictions near the tip show minor grid dependence as a result of the sensitivity of the blade pressure to the position and strength of the tip vortex of the preceding blade. Overall, the results show that CFD simulations using the present multiblock meshes capture the flow features well and can predict the blade loading near the tip and the swept-back section of this rotor.

B.   Nonlifting Model Rotors in High-Speed Flight

This rotor is a modified Alouette helicopter tail rotor tested by ONERA [19,20]. Two different rotor blade configurations are considered, as shown in Fig. 5. One has a nearly straight leading edge and a 75-cm radius. The second configuration has 30-deg leading edge sweep on the outer 15% and a radius of 83.5 cm. The blades used here are different from the ONERA experiment in that the tapered root parts of the blades are removed (i.e., the blade up to 37% radius of the straight blade and 33% radius of the swept-tip blade). Both blades have symmetric NACA four-digit sections, varying in relative thickness from 17% at the root (37% radius of the straight blade and 33% radius of the swept-tip blade) to 9% at the tip. Both blades have a linear taper and the tip chord is 70% of the root chord. The increased blade radius of the swept-tip blade was achieved by adding an 85-mm blade extension of 14.5% relative thickness at 80% radius of the straight blade (i.e., between 71.9 and 82%R of the swept-tip blade). The sweep starts at 85.7%R, at which station the

relative thickness is 13.5%. Based on the root chord, the rotor aspect ratio is 4.518 for the straight blade and 5.03 for the swept-tip blade. Table 2 summarizes the test cases considered in this work. Inviscid time-marching simulations were carried out using a step in the azimuthal direction of 0.25 deg. A detailed time-convergence study showed that the employed step is sufficiently small to capture the unsteadiness of the flow. For validation purposes, two cases at $\mu = 0.45$ (see Table 2) were considered. For a radial station at 90% radius, Fig. 5 shows a comparison between the computed and measured chordwise pressure distributions at five azimuthal stations on the advancing side. For both blade configurations, the correlation of the computed results and the experimental data are very good. For the swept-tip blade, the experimental data show more scatter; however, the comparison with CFD is still favorable.

C.   UH-60A Rotor in High-Speed Flight

This validation test case is the UH-60A main rotor in high-speed forward-flight conditions, corresponding to flight counter 8534 from the U.S. Army/NASA UH-60A Airloads Program [1]. The rotor advance ratio was $\mu = 0.368$, whereas the thrust coefficient was $C_T/\sigma = 0.084$. The rotor blade geometry used here is that from the UH-60A hover test case, described previously (i.e., the wind-tunnel-model geometry of Lorber et al. [2]), scaled to full size and including the elastic torsional deflection from this hover test case. The trim state of the rotor was the converged CFD weak-coupling trim state presented by Potsdam et al. [8]. The elastic torsion was prescribed based on data obtained from the work of Datta et al. [9]. The predicted elastic twist from these authors for the situation with experimentally obtained airloads was scanned, and a curve fit was created with five Fourier modes. Figure 6a presents the torsional deflection from Datta et al. and the corresponding fit. The revolution-averaged deflection was then removed from this fit. The assumption is made that the mean torsional deflection in this forward-flight case is of similar magnitude as the torsional deflection in the hover wind-tunnel condition at

a) Straight-tip blade

b) Swept-tip blade

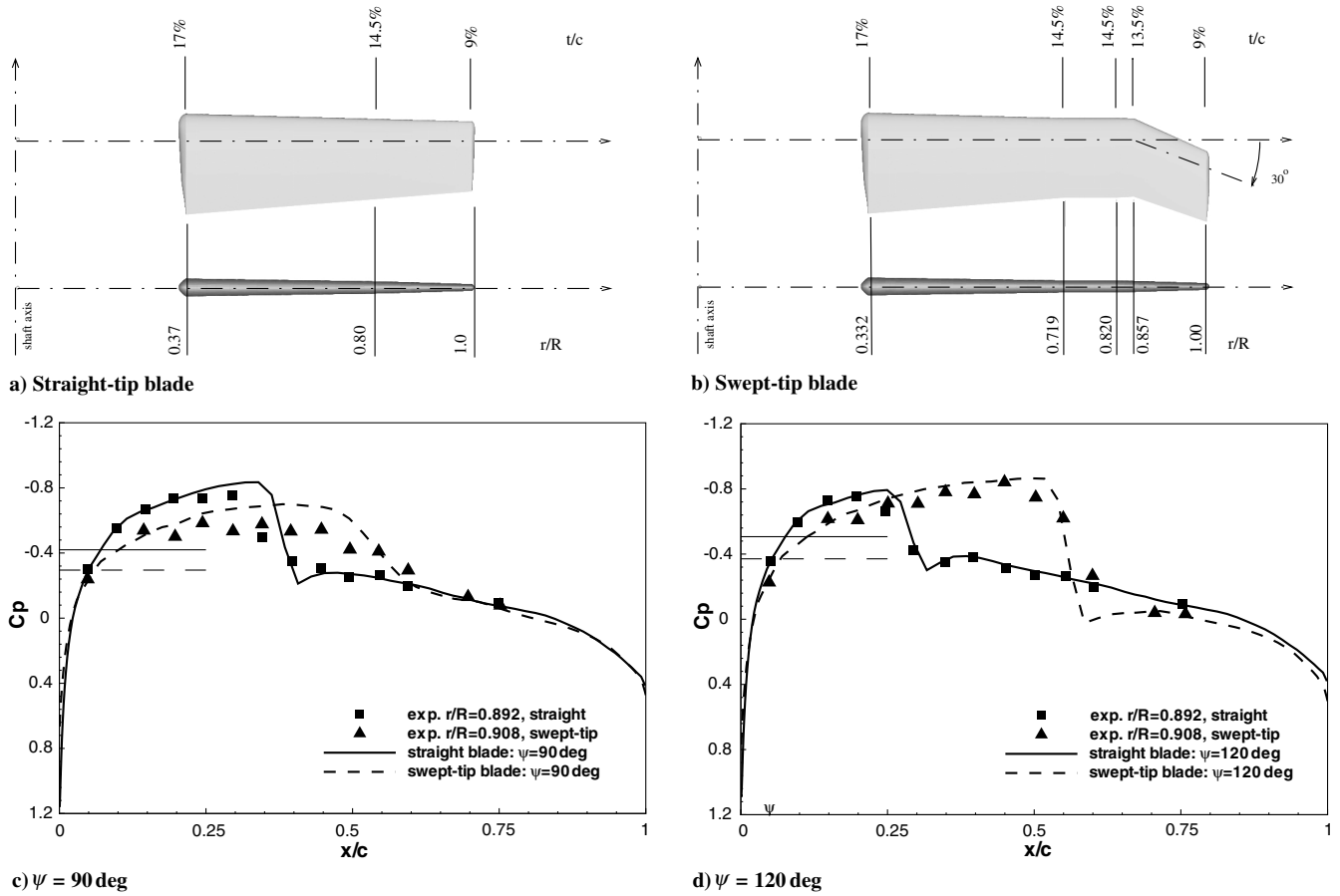c) $\psi = 90\,\mathrm{deg}$

d) $\psi = 120\,\mathrm{deg}$

Fig. 5   Comparison of computed chordwise c_p distribution with the experiment from Philippe and Chattot [19]; nonlifting two-bladed ONERA model rotor [19]; straight-blade and swept-tip blades. The tip Mach number for the straight blade is 0.60, whereas that for the swept-tip blade is 0.628. For both cases, advance ratio $\mu = 0.45$. The solid and dashed horizontal lines correspond to the critical pressure coefficient for the straight-blade and swept-tip blade, respectively.

similar rotor thrust. Furthermore, it is assumed that the elastic torsion varies linearly with rotor radius. Elastic-blade flapping and lead-lag deflections were ignored in the present work. Figures 6b and 6c compare the predicted sectional normal force and pitching moments with the experimental data. The comparison is favorable, considering the uncertainty in the assumed structural response of the rotor. The phasing of the sectional normal force and pitching moments is well-predicted for the present CFD results, with an imposed elastic twist deformation based on the measured airloads. Furthermore, the present CFD approach is capable of predicting the magnitude of the pitching moments on the advancing side of the rotor. Previously, Potsdam et al. [8], as well as Datta et al. [9], showed a similar agreement for their CFD predictions with the flight test data. In the present work, the contribution of the blade twist is quantified by comparing the predictions for an elastic rotor blade with results from a simulation assuming rigid rotor blades.

III.   Results and Discussion

The CFD investigation of the advancing-side lift phase discussed in the present work comprises separate steps, each aiming to quantify specific aspects of the problem, starting with unsteady 2D
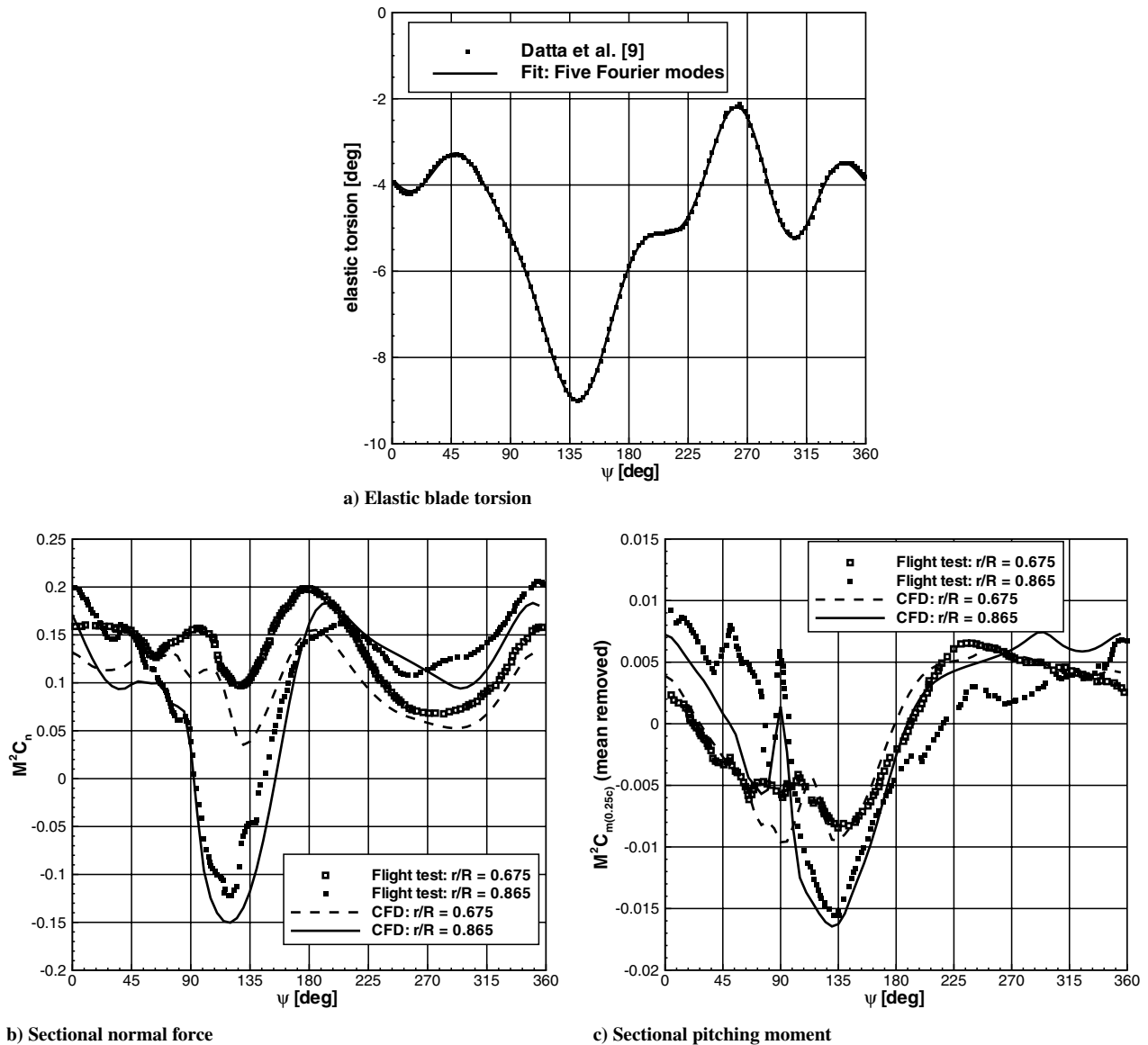
simulations of airfoil sections in oscillatory pitch and translation and concluding with a discussion of three simulations of the UH-60A main rotor in high-speed forward flight with different input parameters to quantity the effects of trim state and elastic-blade torsion. It has to be mentioned that full sets of the UH-60A rotor data are not available in the open literature, and for this reason, data for this rotor had to be obtained from published works [8,9,18].

A.   Two-Dimensional Equivalent: Oscillatory Relative Mach Number and Blade Pitch

The first step of the present investigation aims to quantify the effect of the periodic relative Mach number variations, as well as the combined effects of the relative Mach number and blade pitch variations, experienced by a rotor blade section in forward flight. Neglecting the contributions of rotor shaft inclination and induced flow, the velocity component in the chordwise direction at fraction r/R of the blade span is a function of the blade azimuth and combines a mean velocity equal to r/R times the tip velocity and a sinusoidal variation of amplitude equal to the freestream velocity. This equivalence is sketched in Fig. 1 for the UH-60A main rotor at an advance ratio 0.368. In the equivalent 2D simulations, the reference velocity is the freestream velocity U_∞, and the chord length c

Table 2   Parameters of forward-flight cases considered in the present study

Case	Rotor	μ	M_{tip}	θ_{shaft}	θ_0	θ_{1s}	θ_{1c}	β_0	β_{1s}	β_{1c}
ONERA I	Straight-Tip	0.50	0.625	0.0	0.0	0.0	0.0	0.0	0.0	0.0
ONERA II	Straight-Tip	0.45	0.600	0.0	0.0	0.0	0.0	0.0	0.0	0.0
ONERA III	Swept-Tip	0.45	0.628	0.0	0.0	0.0	0.0	0.0	0.0	0.0
UH-60 baseline	UH-60A	0.368	0.648	7.3	14.6	8.63	−2.39	3.43	−2.04	−0.70
UH-60 red flap	UH-60A	0.368	0.648	7.3	14.6	8.63	−2.39	3.43	−1.04	−0.70
UH-60 elastic	UH-60A	0.368	0.648	7.3	14.6	8.63	−2.39	3.43	−1.04	−0.70

a) Elastic blade torsion

b) Sectional normal force

c) Sectional pitching moment

Fig. 6   Validation results for the UH-60A rotor in high-speed flight: a) prescribed elastic-blade twist, b) sectional normal force, and c) sectional pitching moments.

represents the reference length. Based on these reference values, a reduced frequency can be defined as $k = \omega c/(2U_\infty)$, where ω is the dimensional angular velocity. In terms of rotor parameters, this reduced frequency is defined as $k = 1/(2 \cdot r/R \cdot R/c)$. Based on the freestream velocity and chord length, the nondimensional time $\tilde{t} = tU_\infty/c$ is also defined. The translational motion sketched in Fig. 1c is therefore governed by

$$\frac{\mathrm{d}x_{0.25c}}{\mathrm{d}\tilde{t}} = -\frac{\mu}{r/R}\sin(2k\tilde{t}) \qquad (1)$$

For the rotor sections at 77.5, 86.5, and 92.0%R, the equivalent 2D conditions are presented in Table 1. First, periodic translational motion at a fixed blade pitch is considered for the 77.5 and 92.2%R stations. Figure 1b shows the relative Mach number variation at both stations. The sectional normal force and pitching moment coefficients are presented in Fig. 7. The airfoil incidence is 4.0 and 2.0 deg, for the 77.5 and 92.2%R stations, respectively, approximating the pitch reduction due to the blade twist. Figure 7a shows that the normal force variation lags the relative Mach number variation on the advancing side. This delay is well-reported and occurs in a wide range of conditions, ranging from low-Mach-number essentially incompressible flow to supercritical transonic conditions. The phase delay can be attributed to two effects. First, the time-dependent lift results in a time-dependent wake that advects the

circulation changes. As such, this wake contains the history of the circulation changes. The time-dependent effect of this wake on the flow around the section is the *circulatory* effect. The second contribution is the *impulsive* contribution arising from compressibility effects; that is, the formation of a supersonic pocket of varying chordwise extent and the corresponding varying normal-shock position. The increased delay for the higher-Mach-number outboard station can mainly be attributed to the impulsive effect. The time-dependent chordwise extent of the supersonic pocket and normal-shock location also explain the presence of a sharp nose-down pitching moment peak for the 92.0%R station. For the 77.5%R station, this effect is significantly weaker.

Figure 8 presents the sectional normal force and pitching moment coefficients for the cases with combined oscillatory translation and a pitch schedule derived from the geometric blade incidence for the trim state of the UH-60A rotor in high-speed flight (Table 2). This pitch schedule combines the contributions due to the blade flapping and pitching as well as rotor shaft forward inclination. Induced flow and crossflow effects cannot be included. Similar to the fixed-pitch cases, the normal force variation lags the imposed flowfield conditions; in this case, the relative Mach number as well as the blade pitch variation. Again, the effect is more significant further outboard.

Figures 9 and 10 present the extent of supersonic flow for the 77.5 and 92.0%R stations, respectively. The supersonic regions in these
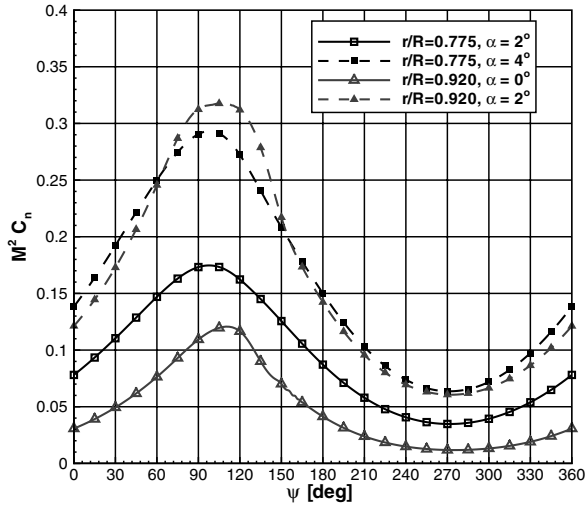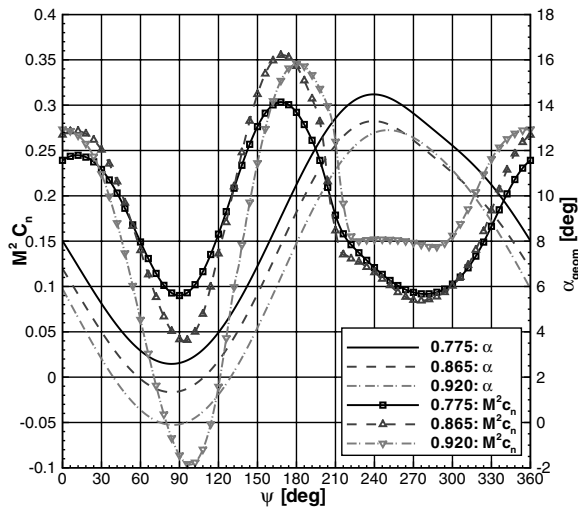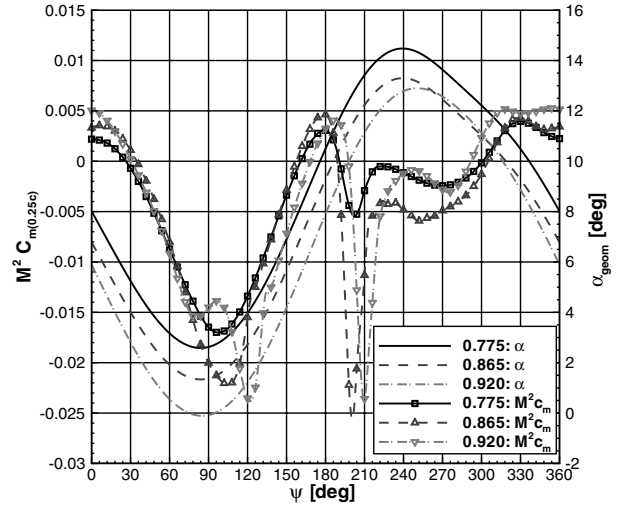
a) Sectional normal force
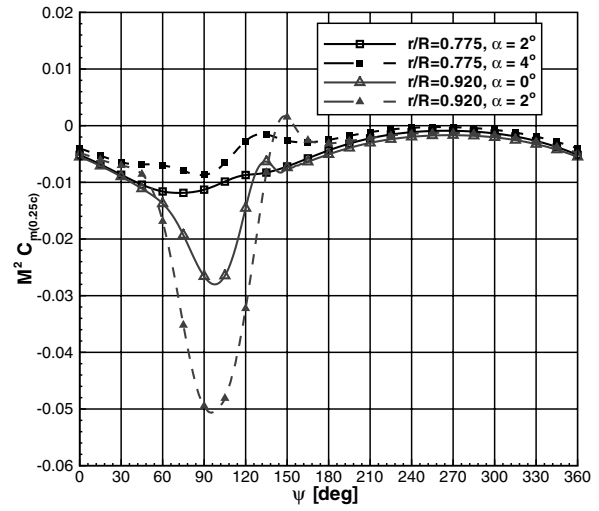
b) Sectional pitching moment
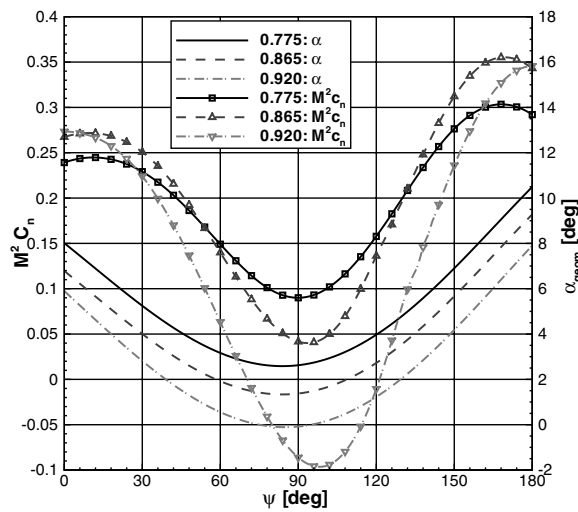
Fig. 7   Sectional normal force and pitching moment coefficient for the SC1095R8 section ($r/R = 0.775$) and SC1095 section ($r/R = 0.920$); oscillatory translation; $Re = 4 \times 10^6$; and k-ω turbulence model. Details of the conditions are given in Table 1.
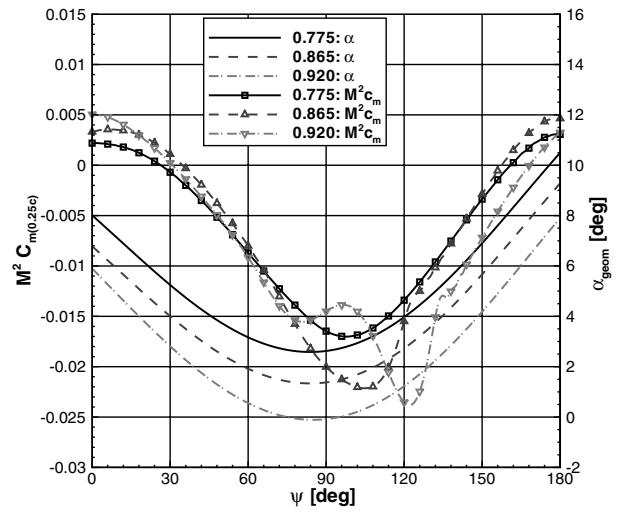

a) Normal force coefficient

b) Pitching moment coefficient

c) Normal force coefficient

d) Pitching moment coefficient

Fig. 8   Sectional normal force and pitching moment coefficient for the SC1095R8 section ($r/R = 0.775$) and SC1095 section ($r/R = 0.865$ and $r/R = 0.920$); combined freestream Mach number/pitch oscillation; $Re = 4 \times 10^6$; and k-ω turbulence model. The detailed conditions are given in Table 1.
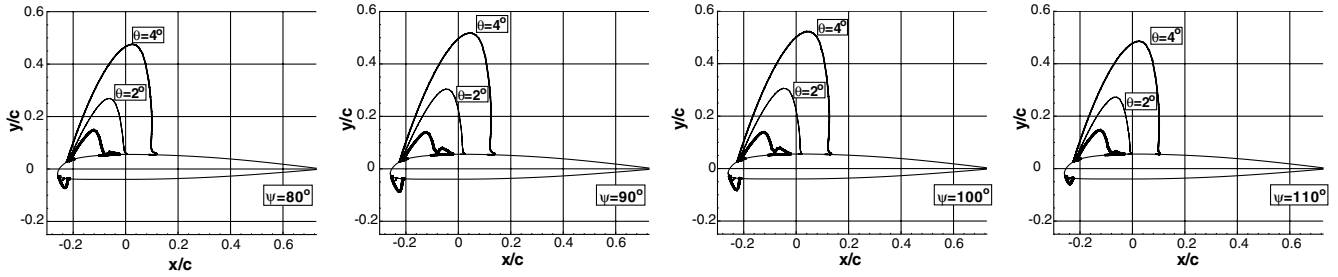
Fig. 9 Sonic lines obtained from the ratio of pressure and isentropic critical pressure; SC1095R8 section in oscillatory translational motion. The conditions approximate the Mach number schedule of blade station 77.5%R of UH-60A rotor at $\mu = 0.368$. The following cases are shown: fixed pitch of 2 deg (thin line), fixed pitch at 4 deg (solid line), and pitch schedule from geometric incidence on rotor (thick line). More details of the conditions can be found in Table 1.
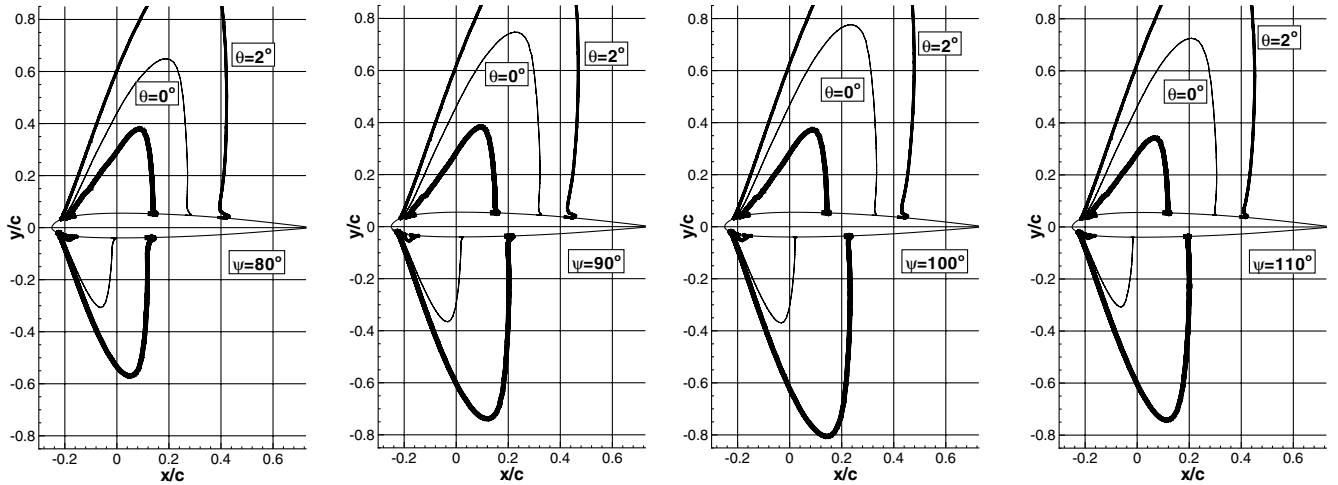

Fig. 10 Sonic lines obtained from the ratio of pressure and isentropic critical pressure; SC1095 section in oscillatory translational motion. The conditions approximate the Mach number schedule of blade station 92.0%R of UH-60A rotor at $\mu = 0.368$. Three cases are shown: fixed pitch of 0 deg (thin line), fixed pitch at 2 deg (solid line), and pitch schedule from geometric incidence on the rotor (thick line). Conditions for the CFD computations are given in Table 1.

figures are determined from the ratio of static pressure to critical pressure. At both stations, results are compared against the combined pitch/translation data. The fixed-pitch cases show a hysteresis of the solution at about the azimuth angle at which the maximum relative Mach number occurs (i.e., at $\psi = 80$ and 100 deg, the same relative Mach number is experienced), whereas the solutions are distinctly different. This hysteresis is consistent with the phase lag of the blade lift relative to the relative Mach number variation. The nonlifting rotors discussed in the next section show a similar hysteresis for the chordwise extent of supersonic flow. For the pitch/translation case at 92.0%R, between 80- and 90-deg azimuth, the supersonic flow extent on the lower surface exceeds that on the upper surface. This crossover coincides with a local change in slope of the pitching moment curve. For the 77.5%R station, the Mach number and therefore the extent of supersonic flow are significantly smaller. Similarly, the hysteresis and phase lag of lift and moment are smaller than for the 92.0%R station.

Table 3 presents a summary of the obtained results in terms of the phase delay. As can be seen, the trend of the obtained data are consistent with the preceding observations regarding the effect of the Mach number, with larger delay values obtained at higher Mach. This trend is maintained for the cases of higher advance ratio as well as for the case of higher oscillation frequency.

B. Nonlifting Rotors: Three-Dimensional Crossflow and Tip Effects

The following step of the investigation aims to quantify the effects of 3D crossflow and finite span in addition to the relative Mach number variations studied in the previous section. To eliminate the effect of a complex inflow field, a nonlifting rotor at high-speed flight is considered. The nonlifting ONERA [19,20] rotors at $\mu = 0.45$ and 0.50, as previously described in Sec. II.B, are used. For nonlifting cases, delay effects on the blade pressure from the time-dependent

advected wake are absent. Figure 11 shows the variation of chordwise c_p versus azimuth for the two blades at conditions given in Table 2. Results are shown at two radial stations (85 and 90%R).

Figures 11a and 11b present the results for the straight-tip blade at $\mu = 0.45$. The plots clearly show a hysteresis of the chordwise extent of supersonic flow and normal shock position with blade azimuth ψ (i.e., the pressure distributions at $\psi = 60$ and 120 deg are very different), despite the identical blade-normal Mach numbers. The station further outboard (90% rotor radius) experiences higher Mach numbers. Because the cases are nonlifting, the observed delays cannot be attributed to circulatory effects.

Results for the straight-tip blade at $\mu = 0.50$ are shown in Figs. 11c and 11d, compared with the results at $\mu = 0.45$. The

Table 3 Phase delay of sectional lift minimum for SC1095 in combined translation/pitching motion

M_∞	M_{min}	M_{max}	Phase delay, deg
$\lambda = 0.40$, $\alpha = 4$ deg -4 deg $\sin(2$ kt$)$, $k = 0.05$.			
0.45	0.270	0.630	6
0.50	0.300	0.700	7
0.55	0.330	0.770	8
0.60	0.360	0.840	12
0.65	0.390	0.910	16
$\lambda = 0.50$, $\alpha = 4$ deg -4 deg $\sin(2$ kt$)$, $k = 0.05$.			
0.45	0.225	0.675	6
0.50	0.250	0.750	7.5
0.55	0.275	0.825	11
0.60	0.300	0.900	15
$\lambda = 0.50$, $\alpha = 4$ deg -4 deg $\sin(2$ kt$)$, $k = 0.10$.			
0.50	0.250	0.750	8
0.55	0.275	0.825	11
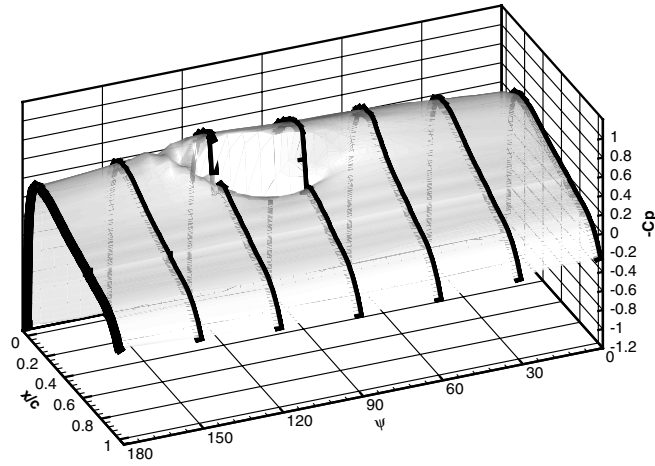
a) Straight-tip blade: $M_{tip} = 0.60$, $\mu = 0.45$, and $r/R = 0.85$
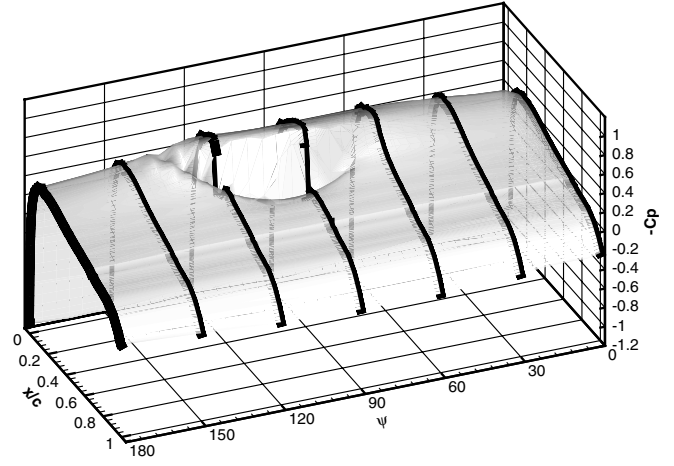
b) Straight-tip blade: $M_{tip} = 0.60$, $\mu = 0.45$, and $r/R = 0.90$
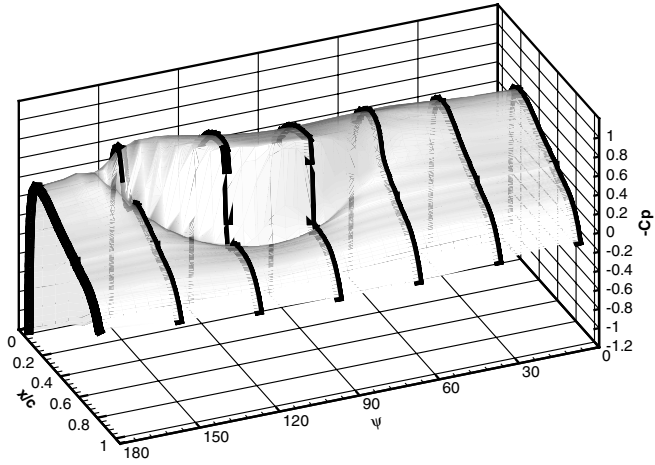
c) Straight-tip blade: $M_{tip} = 0.625$, $\mu = 0.50$, and $r/R = 0.85$
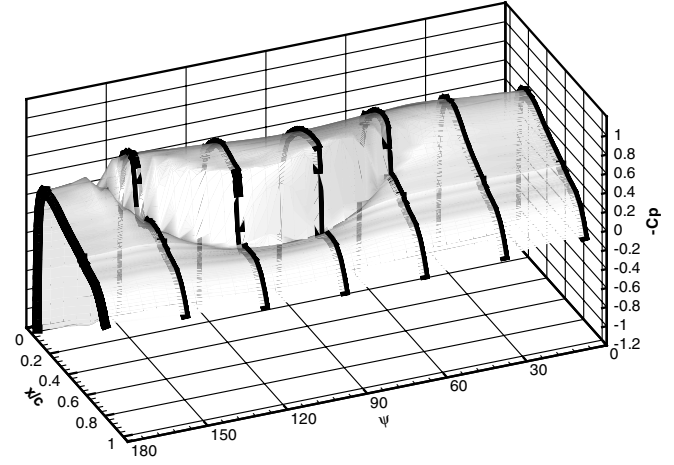
d) Straight-tip blade: $M_{tip} = 0.625$, $\mu = 0.50$, and $r/R = 0.90$.
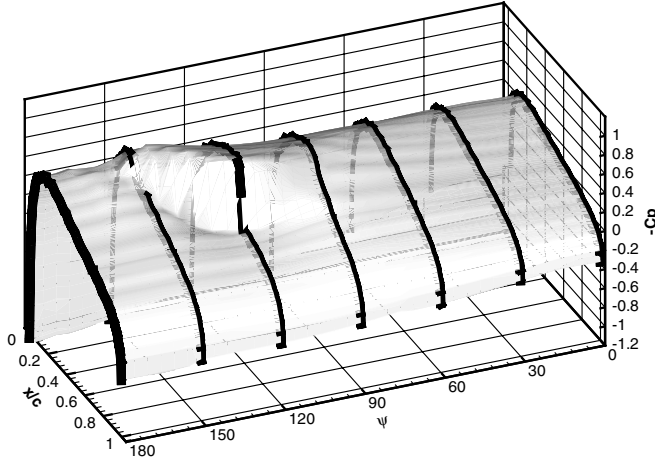
e) Straight-tip blade: $M_{tip} = 0.628$, $\mu = 0.45$, and $r/R = 0.85$
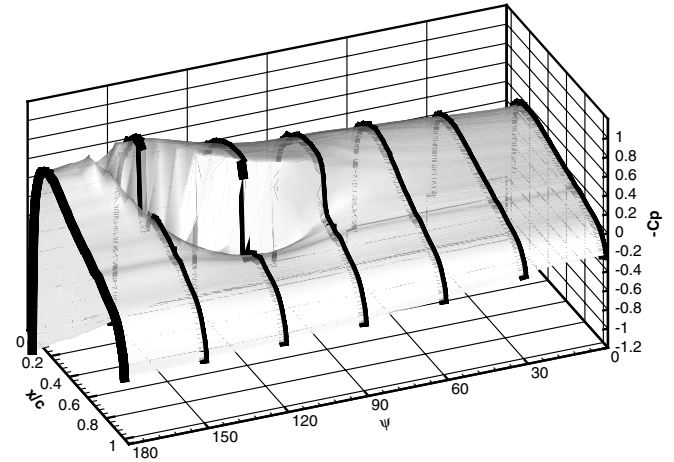
f) Swept-tip blade: $M_{tip} = 0.628$, $\mu = 0.45$, and $r/R = 0.90$

Fig. 11   Chordwise c_p as function of azimuth for the nonlifting ONERA model rotor equipped with its straight-tip and swept-tip blades.

increased advance ratio and higher tip Mach number leads to stronger normal shocks and the shock positions are further aft. Furthermore, the hysteresis in the pressure variation with azimuth is increased. For the 85% radial station, the normal shock forms at around $\psi = 60$ deg and is still present at $\psi = 150$ deg. The results for the swept-tip blade at $\mu = 0.45$ show stronger shocks than for the straight-tip blade at this advance ratio, which can be attributed to the higher tip Mach number. The relief of compressibility effects due to the tip sweep does not fully compensate for this higher tip Mach number. Around $\psi = 90$ deg, the tip sweep clearly reduces the shock strength, but now a stronger shock occurs at larger blade

azimuth ψ. The stronger hysteresis in the surface pressure distribution for the swept-tip blade can be explained from geometric considerations, because the tip-sweep delays the maximum blade-normal Mach numbers to larger values of ψ. The added phase shift relative to the straight-tip blade results is similar to the tip-sweep angle.

In the case of a lifting rotor, the situation is significantly more complicated due to the presence of a three-dimensional inflow field. Furthermore, circulatory effects will be present, along with the impulsive effect analyzed here. These observations led to further computations as discussed in the next section.

C. UH-60A Rotor in High-Speed Forward Flight

The isolated main rotor of the UH-60A in high-speed forward flight is considered in this section at an advance ratio of 0.368, corresponding to the helicopter flying at approximately 155 kt, whereas the rotor loading is $C_T/\sigma = 0.08$. This condition corresponds to flight counter 8534 in the UH-60A Airloads Program. The trim state used here was obtained from combining literature data [8,9,21]. The details of the considered test case are presented in Table 2.

The multiblock structured grids for the Navier–Stokes simulations contained a total of 7,900,000 cells in 992 grid blocks. A C-H topology was used in the chordwise direction, along with wall spacings of $2.0 \times 10^{-5}c$ for the first cell on the blade surface. The grid had 95 grid points in the radial, 50 in the wall-normal, and 150 in the wraparound directions. The rotor hub is modeled as a generic ellipsoidal surface. All simulations in this section employed a time step corresponding to 0.25 deg in the azimuthal direction. From the experience gained with the nonlifting rotors, this step size is sufficiently small to resolve the unsteadiness of the supersonic flow region and normal shocks.

Based on the trim state specified in Table 2, the geometric incidence for the 0.675, 0.775, 0.865, and 0.920R stations is presented in Figs. 12a and 12b. The figures compare the rigid-blade trim state with $\beta_s = -1.0$ deg with the prescribed elastic torsion case, which assumes a linearly elastic torsion dependence in the blade spanwise direction and is based on the curve fit with five Fourier modes of the torsional deflection reported by Datta et al. [9]. The comparison shows that for the rigid-blade case, the minimum sectional geometric incidence occurs close to $\psi = 90$ deg for the considered stations. Introduction of the elastic torsion can be seen to shift this minimum to azimuth angles of 115 deg. Furthermore, at the rear of the rotor disk, the torsional deflection is nose-up. On the advancing side of the rotor, the blade sections experience a strong nose-down pitching moment, followed by a nose-down torsional repose, which reaches a maximum around $\psi = 135$ deg.

Figures 13a–13f show the sectional normal force and pitching moments coefficients for the 0.675, 0.865, and 0.920R stations for the three test cases. The results from the test case with prescribed torsional deflection show a good agreement with the experimental results, considering the uncertainty in the applied structural response of the rotor. The phasing and magnitude of the normal force and pitching moment coefficients are captured well. For the rigid-blade cases, the missing contribution to the sectional incidence of torsional response leads to an inaccurate prediction of the sectional normal force on the advancing side of the rotor, in magnitude and phasing.

The normal force minimum for the outboard station 0.920R lags the geometric sectional incidence by around 8 deg in azimuth, which is consistent with the normal force delays found in the 2D unsteady simulations for comparable conditions. Hence, this can be mainly attributed to the compressibility effects. For the simulation assuming elastic-blade torsion, the delay of the normal force minimum is around 5–8 deg for the outboard stations. The pitching moment coefficients for the rigid-blade simulations have the correct magnitude, which can be explained by the fact that the strong nose-down moments are caused by unsteady compressibility effects that are presented regardless of incidence variations resulting from elastic deformations. The phase discrepancy of the pitching moments with the experimental data for the rigid-blade cases is consistent with the different blade incidence phasing shown in Figs. 12a and 12b for the rigid-blade and elastic-blade cases. The phasing of the pitching moments shows a delay relative to the blade incidence of around 25 deg for the outboard stations, which is consistent with the unsteady 2D simulations discussed previously. This effect can be attributed to unsteady compressibility effects. The phase delay can be explained by the delay in attaining the maximum extent of supersonic flow, as is apparent from the results for the nonlifting rotor discussed previously. This effect increases with increasing relative Mach number; that is, the effect is more pronounced further outboard. Also presented in Figs. 13a–13f is a comparison of rigid-blade simulations with the trim state from Potsdam et al. [8] and one with a reduced-flapping deflections. These results are compared to show the sensitivity of the rotor airloads to trim-state variations. The reduction of the blade flapping on the advancing side shifts the sectional incidence minimum by 5–10 deg in azimuth and reduces the incidence at the front of the rotor disk. The normal force and pitching moment for the reduced-flapping case show a phase shift consistent with the blade incidence shift. The effect of the reduced flapping can be seen to be secondary to blade torsion effects. Table 4 presents the obtained results and the associated lift-phase delays.

In summary, the results for the high-speed flight conditions show that the magnitude of the pitching moment on the advancing side can be predicted with reasonable accuracy regardless of rigid-blade assumptions. Furthermore, the phase delay of the unsteady sectional airloads relative to the sectional incidence schedule is not affected by elastic torsional response and is consistent with those found in unsteady 2D simulations at comparable conditions. The phasing of the pitching moment and normal force coefficients, as well as the normal force magnitudes, are evidently sensitive to the structural response of the blade in torsion, as can be expected from previous work by Potsdam et al. [8] and Datta et al. [9], among others.
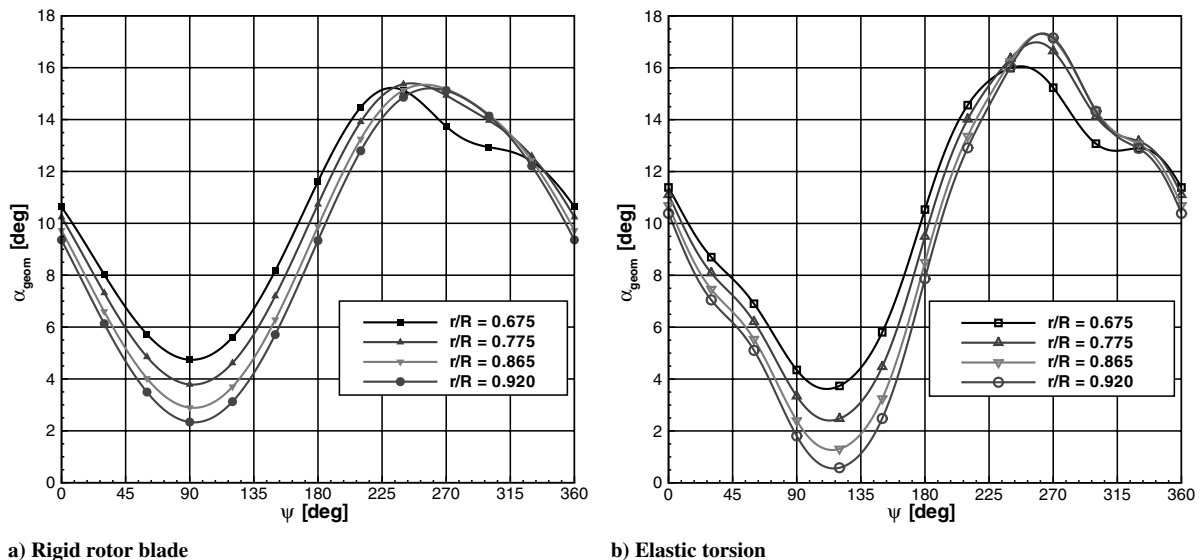

a) Rigid rotor blade   b) Elastic torsion

Fig. 12 Geometric section incidence for UH-60A main rotor in high-speed flight ($\mu = 0.368$, $M_{tip} = 0.642$, $\theta_0 = 14.6$ deg, $\theta_{1s} = 8.63$ deg, $\theta_{1c} = -2.39$ deg, $\beta_0 = 3.43$ deg, $\beta_{1s} = -1.0$ deg, $\beta_{1c} = -0.70$ deg, and $C_T/\sigma = 0.08$). For the considered stations, the elastic-blade torsion leads to a shift of the azimuth angle at which the sectional incidence reaches its minimum from close to 90 to around 115 deg.
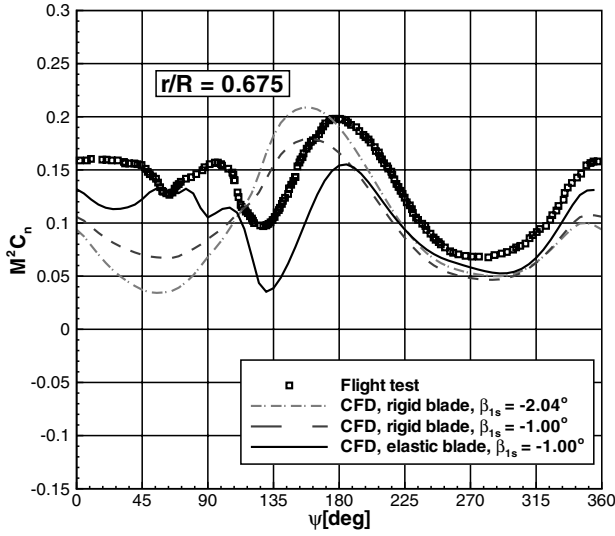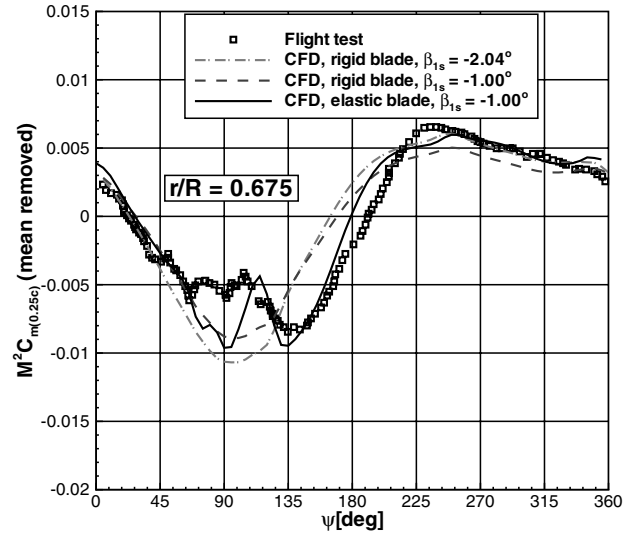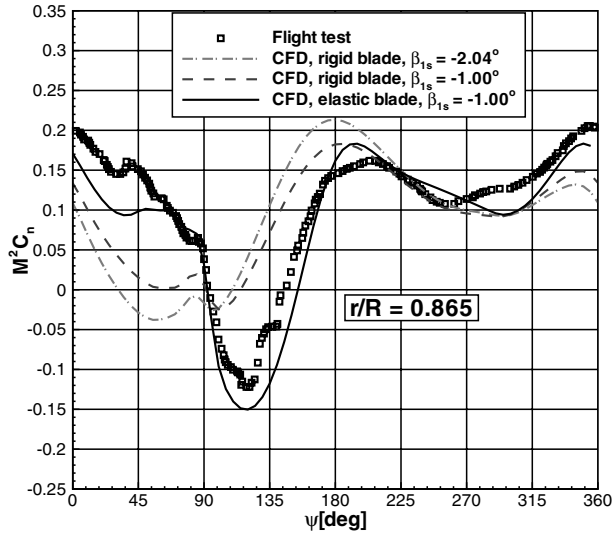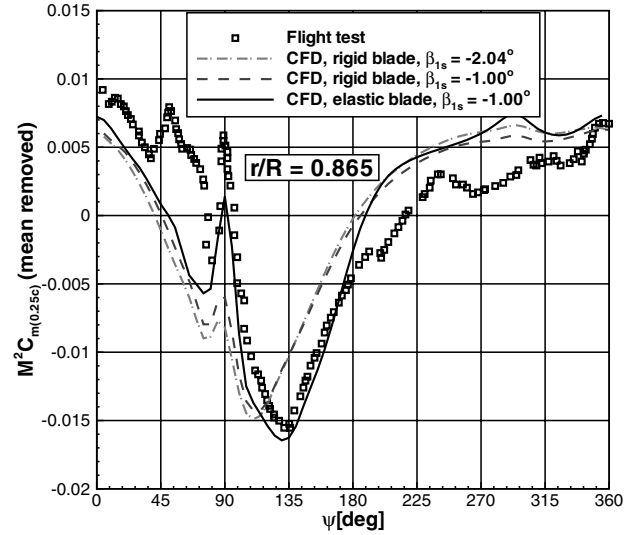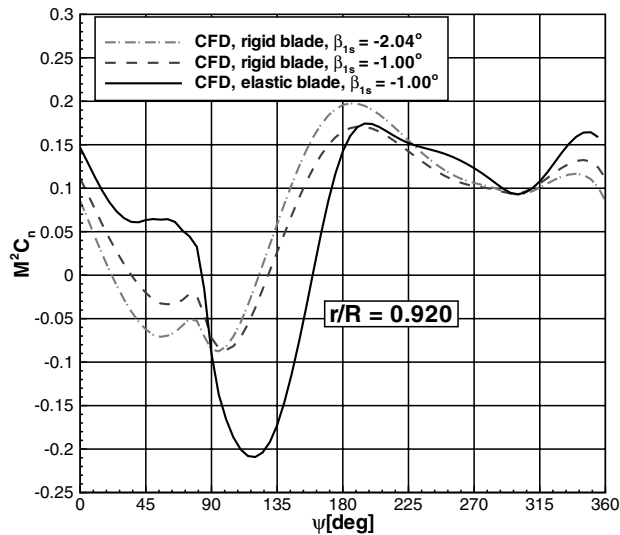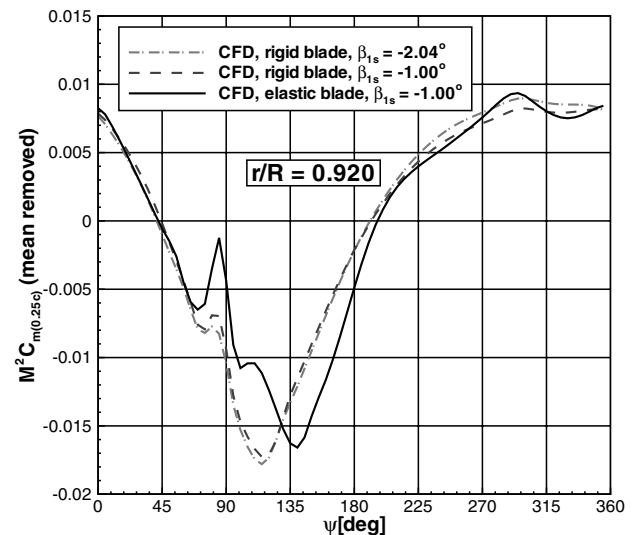
a) Sectional normal force, *r/R* = 0.675

b) Sectional pitching moment, *r/R* = 0.675

c) Sectional normal force, *r/R* = 0.865

d) Sectional pitching moment, *r/R* = 0.865

e) Sectional normal force, *r/R* = 0.920

f) Sectional pitching moment, *r/R* = 0.920

Fig. 13   Azimuthal variation of the sectional normal force and pitching moments for the UH-60A rotor in high-speed forward flight ($\mu = 0.368$, $M_{tip} = 0.642$, $\theta_0 = 14.6\,\text{deg}$, $\theta_{1s} = 8.63\,\text{deg}$, $\theta_{1c} = -2.39\,\text{deg}$, $\beta_0 = 3.43\,\text{deg}$, $\beta_{1s} = -2.04\,\text{deg}$, $\beta_{1c} = -0.70\,\text{deg}$, and $C_T/\sigma = 0.08$).

Table 4 Phase delay of sectional lift and moment for UH-60A main rotor in forward flight; azimuthal angles for minimum geometric pitch, sectional normal force and sectional pitching moment coefficients are compared

Case	$r/R = 0.775$			$r/R = 0.865$			$r/R = 0.920$		
	θ, deg	M^2C_n, deg	M^2C_M, deg	θ, deg	M^2C_n, deg	M^2C_M, deg	θ, deg	M^2C_n, deg	M^2C_M, deg
UH-60 baseline	84	60	85	85	95	110	85	95	115
UH-60 red.flap	92	62	85	93	100	115	93	100	117
UH-60 elastic	113	120	120	115	120	130	116	120	140

IV. Conclusions

A CFD investigation of the advancing-side lift-phase delay was conducted. Separate aspects of the unsteady flowfield were analyzed, including compressibility, freestream Mach number oscillation, yawed flow, and finite span effects. Two-dimensional simulations were conducted to quantify the effect of compressibility and freestream Mach number oscillation on the phasing of the lift and pitching moment coefficients. The results for the freestream Mach number oscillations show that the lift coefficient lags the Mach changes at outboard stations (by approximately 8 and 15 deg for the 77.5- and 92.5-deg stations, respectively). For the combined freestream Mach number/pitch oscillations, the phase delay is reduced to around 5 deg for the 77.5% and 8 deg for the 92.5% station.

Finite span and sideslip contributions to the phasing were quantified by investigating the chordwise extent of supersonic flow on the advancing side for two nonlifting rotors in high-speed flight. It was found that for the high-speed cases considered, the chordwise extend of supersonic flow shows a hysteresis relative to the $\psi = 90$- deg position of 10–15 deg. For the nonlifting rotor cases, this is a combined effect of compressibility, relative Mach number variation, and crossflow, because induced flow and wake effects are not present.

Finally, the UH-60A rotor in high-speed forward flight was considered. By comparing results for rigid blades with results for a prescribed blade torsional deflection, the contribution of the blade torsion to the advancing-blade lift phasing was also quantified. Furthermore, rigid-blade simulations with different flapping schedules demonstrated the sensitivity of the lift phasing to trim-state variations. It was found that the contribution due to torsional deflections is far more significant than blade-flapping changes of similar magnitude. The elastic torsional deflection of the blades effectively changes the pitch schedule of the blade sections and therefore plays a dominant role in the phasing of the lift and pitching moment coefficients. The delayed response of the blade airloads to pitch changes is mainly Mach-number-dependent. Interestingly, the rotor calculations predicted the lift minimum for inboard sections of the rotor at a higher azimuth than the 2D results, whereas moving outboard, the differences between rotor calculation and the 2D cases were reduced, and at stations close to the tip, the situation was reversed, with the 2D results lagging behind in phase, in comparison with the rotor.

Acknowledgments

References

[1] Kufeld, R., Balough, D., Cross, J., Studebaker, K., and Jennison, C., "Flight Testing the UH-60A Airloads Aircraft," *American Helicopter Society 50th Annual Forum*, AHS International, Alexandria, VA, May 1994.

[2] Lorber, P., Stauter, R., and Landgrebe, A., "A Comprehensive Hover Test of the Airloads and Airflow of an Extensively Instrumented Model Helicopter Rotor," *American Helicopter Society 45th Annual Forum*, AHS International, Alexandria, VA, May, 1989.

[3] Lorber, P., "Aerodynamic Results of a Pressure-Instrumented Model Rotor Test at the DNW," *Journal of the American Helicopter Society*, Vol. 36, No. 4, 1991, pp. 66–76.

[4] Conlisk, A., "Modern Helicopter Aerodynamics," *Annual Review of Fluid Mechanics*, Vol. 29, Jan. 1997, pp. 515–567.
doi:10.1146/annurev.fluid.29.1.515

[5] Coleman, C., and Bousman, W., "Aerodynamic Limitations of the UH-60A Rotor," NASA TM-110396, 1996.

[6] Kufeld, R., and Bousman, W., "UH-60A Airloads Program Azimuth Reference Correction," *Journal of the American Helicopter Society*, Vol. 50, No. 2, 2005, pp. 211–213.

[7] Bousman, W., "Putting the Aero Back into Aeroelasticity," NASA TM-2000-209589, Mar. 2000.

[8] Potsdam, M., Yeo, H., and Johnson, W., "Rotor Airloads Prediction Using Loose Aerodynamic/Structural Coupling," *Journal of Aircraft*, Vol. 43, No. 3, 2006, pp. 732–742.

[9] Datta, A., Sitaraman, J., Chopra, I., and Baeder, J., "CFD/CSD Prediction of Rotor Vibratory Loads in High-Speed Flight," *Journal of Aircraft*, Vol. 43, No. 6, 2006, pp. 1698–1709.

[10] Favier, D., Agnes, A., Barbi, C., and Maresca, C., "Combined Translation/Pitch Motion: A New Airfoil Dynamic Stall Simulation," *Journal of Aircraft*, Vol. 25, No. 9, 1988, pp. 805–814.

[11] Krause, E., and Schweitzer, W., "The Effect of an Oscillatory Freestream-Flow on a Naca-4412 Profile at Large Relative Amplitudes and Low Reynolds Numbers," *Experiments in Fluids*, Vol. 9, No. 3, 1990, pp. 159–166.

[12] Morikawa, K., and Grönig, H., "Formation and Structure of Vortex Systems Around a Translating and Oscillating Airfoil," *Zeitschrift für Flugwissenschaften und Weltraumforschung*, Vol. 19, No. 6, 1995, pp. 391–396.

[13] Datta, A., and Chopra, I., "Validation of Structural and Aerodynamic Modeling Using UH-60A Flight Test Data," *American Helicopter Society 59th Annual Forum*, AHS International, Alexandria, VA, May 2003.

[14] Sitaraman, J., Baeder, J., and Chopra, I., "Validation of UH-60A Rotor Blade Aerodynamic Characteristics Using CFD," *American Helicopter Society 59th Annual Forum*, AHS International, Alexandria, VA, May 2003.

[15] Steijl, R., Barakos, G., and Badcock, K., "A Framework for CFD Analysis of Helicopter Rotors in Hover and Forward Flight," *International Journal for Numerical Methods in Fluids*, Vol. 51, No. 8, 2006, pp. 819–847.
doi:10.1002/fld.1086

[16] Morvant, R., Badcock, K., Barakos, G., and Richards, B., "Aerofoil-Vortex Interaction Using the Compressible Vorticity Confinement Method," *AIAA Journal*, Vol. 43, No. 1, 2005, pp. 63–75.

[17] Spentzos, A., Barakos, G., Badcock, k., Richards, B., Wernert, P., Schreck, S., and Raffel, M., "Investigation of Three-Dimensional Dynamic Stall Using Computational Fluid Dynamics," *AIAA Journal*, Vol. 43, No. 5, 2005.

[18] Dindar, M., Shephard, M., Flaherty, J., and Jansen, K., "Adaptive CFD Analysis for Rotorcraft Aerodynamics," *Computer Methods in Applied Mechanics and Engineering*, Vol. 189, 2000, pp. 1055–1076.
doi:10.1016/S0045-7825(99)00368-0

[19] Philippe, J., and Chattot, J., "Experimental and Theoretical Studies on Helicopter Blade Tips at ONERA," Sixth European Rotorcraft and Powered Lift Aircraft Forum, ONERA Rept. 1980-96, Sept. 1980.

[20] Tauber, M., Chang, I., Caughey, D., and Philippe, J., "Comparison of Calculated and Measured Pressures on Straight and Swept-Tip Model Rotor Blades," NASA TM-85872, 1983.

[21] Yeo, H., and Johnson, W., "Assessment of Comprehensive Analysis Calculation of Airloads on Helicopter Rotors," *Journal of Aircraft*, Vol. 42, No. 5, 2005, pp. 1218–1228.